



Science Arts & Métiers (SAM)

is an open access repository that collects the work of Arts et Métiers Institute of Technology researchers and makes it freely available over the web where possible.

This is an author-deposited version published in: <https://sam.ensam.eu>
Handle ID: <http://hdl.handle.net/10985/24924>

To cite this version :

Hongguang LIU, Mehdi CHERIF, Madalina CALAMAZ, Hélène L. ELIAS-BIREMBAUX, Frederic ROSSI, Gerard POULACHON, Yessine AYED - Progressive damage induced degradation of mechanical properties in the hole surfaces during drilling processes of CFRP - In: CIRP Conference on Surface Integrity, France, 2023 - CIRP Annals - 2023

Any correspondence concerning this service should be sent to the repository

Administrator : scienceouverte@ensam.eu



when $\sigma_{11} < 0$, it yields fiber compressive mode as Eq. (2)

$$e_{ft} = \left(\frac{\sigma_{11}}{X_t}\right)^2 + \left(\frac{\sigma_{12}}{S_{12}}\right)^2 + \left(\frac{\sigma_{13}}{S_{13}}\right)^2 \geq 1 \quad (1)$$

$$e_{fc} = \left|\frac{\sigma_{11}}{X_c}\right| \geq 1 \quad (2)$$

where e_{ft} and e_{fc} denote damage initiation criteria for fiber tensile and compressive modes, respectively. Once their values exceed 1, related damage initiates and starts to accumulate. X_t , X_c , S_{12} and S_{13} are axial tensile strength, axial compressive strength, longitudinal shear strength and transverse shear strength.

2.2. Matrix damage model

In this study, Hou's model is used to calculate damage initiation for matrix [6], which is also composed of tensile and compressive modes. When $\sigma_{22} > 0$, it follows matrix tensile mode as Eq. (3) and when $\sigma_{22} < 0$, it follows matrix compressive mode as Eq. (4)

$$e_{mt} = \left(\frac{\sigma_{22}}{Y_t}\right)^2 + \left(\frac{\sigma_{12}}{S_{12}}\right)^2 + \left(\frac{\sigma_{23}}{S_{23}}\right)^2 \geq 1 \quad (3)$$

$$e_{mc} = \frac{1}{4} \left(\frac{-\sigma_{22}}{S_{12}}\right)^2 + \frac{Y_c^2 \sigma_{22}}{4S_{12}^2 Y_c} - \frac{\sigma_{22}}{Y_c} + \left(\frac{\sigma_{12}}{S_{12}}\right)^2 \geq 1 \quad (4)$$

Similar as fiber damage models, e_{mt} and e_{mc} are used to define damage initiations of the matrix. Y_t and Y_c are transverse tensile strength and transverse compressive strength, respectively.

2.3. Damage evolution law

Damage starts to accumulate following the evolution law once it initiates. Depending on different damage modes, it is calculated separately and accordingly. The dissipated energy G_I follows Eq. (5):

$$G_I = \frac{1}{2} \sigma_{eq}^f \varepsilon_{eq}^f l_c, \quad I = ft, fc, mt, \text{ and } mc \quad (5)$$

where the subscript I denotes different damage modes, l_c is the characteristic length, σ_{eq}^f and ε_{eq}^f are equivalent peak stress and equivalent failure strain, respectively. Then the damage variable is updated following Eq. (6) as

$$d_I = \frac{\delta_{I,eq}^f (\delta_{I,eq} - \delta_{I,eq}^0)}{\delta_{I,eq} (\delta_{I,eq}^f - \delta_{I,eq}^0)}, \quad I = ft, fc, mt, \text{ and } mc \quad (6)$$

where $\delta_{I,eq}^f$ is the full damage equivalent displacement of the corresponding failure mode, $\delta_{I,eq}^0$ is the equivalent displacement at which the failure criterion is satisfied. Detailed explanations of pertinent variables are narrated as proposed in Ref. [6]. Following, the degraded stiffness matrix yields Eq. (7) as

$$\begin{cases} C_{11} = (1 - d_f) C_{11}^0 \\ C_{22} = (1 - d_f)(1 - d_m) C_{22}^0 \\ C_{33} = (1 - d_f)(1 - d_m) C_{33}^0 \\ C_{23} = (1 - d_f)(1 - d_m) C_{23}^0 \\ C_{13} = (1 - d_f)(1 - d_m) C_{13}^0 \\ G_{12} = (1 - d_f)(1 - s_{mt} d_{mt})(1 - s_{mc} d_{mc}) G_{12}^0 \\ G_{23} = (1 - d_f)(1 - s_{mt} d_{mt})(1 - s_{mc} d_{mc}) G_{23}^0 \\ G_{31} = (1 - d_f)(1 - s_{mt} d_{mt})(1 - s_{mc} d_{mc}) G_{31}^0 \end{cases} \quad (7)$$

This model is realized through self-coded subroutine VUMAT with Abaqus/Explicit following the flowchart described in Fig. 1.

2.4. Interfacial damage

Damage at interface, which is always referred as delamination, is modelled through embedding cohesive elements between plies with the traction-separation law. Damage initiation is determined by a

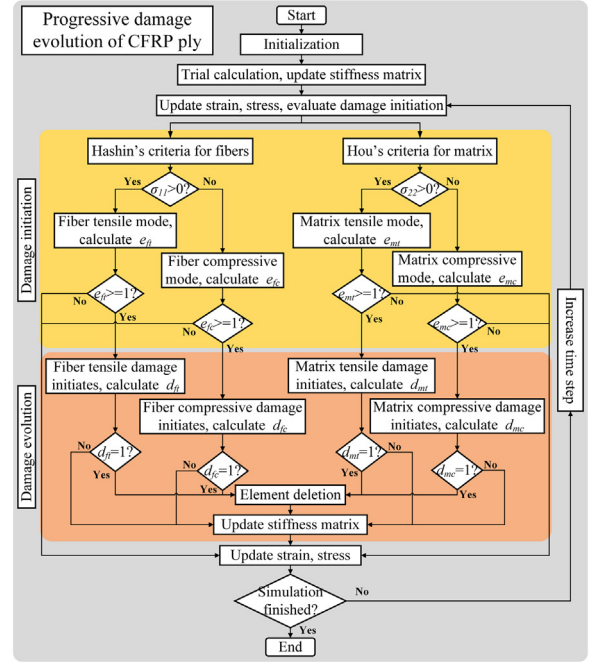


Fig. 1. Flowchart of subroutine with progressive damage evolution laws.

quadratic nominal stress criterion as Eq. (8)

$$\left(\frac{t_n}{t_n^0}\right)^2 + \left(\frac{t_s}{t_s^0}\right)^2 + \left(\frac{t_t}{t_t^0}\right)^2 = 1 \quad (8)$$

where t_n denotes the traction normal stress, while t_s and t_t for shear stresses. A second-order power law is applied to account for the damage evolution based on fracture energies following Eq. (9)

$$\left(\frac{G_n}{G_n^c}\right)^2 + \left(\frac{G_s}{G_s^c}\right)^2 + \left(\frac{G_t}{G_t^c}\right)^2 = 1 \quad (9)$$

where G_n , G_s and G_t denote the work of pertinent direction and the superscript c denotes the critical fracture energy.

3. Experimentation and numerical simulation

3.1. Experimentation

In this study, a multi-directional T800/M21 CFRP plate with thickness of 5 mm was used. A carbide drill with diameter of 5 mm and edge radius around 10 μm provided by Tivoly was applied with a constant cutting speed of 100 m/min. Two different feeds of 0.05 mm/rev and 0.1 mm/rev were used. Drilling tests were performed on HURCO VMX42UHSi 5-axis milling machine and repeated 3 times for each. Cutting forces were measured through rotary dynamometer Kistler 9170A. The set-up is as shown in Fig. 2.

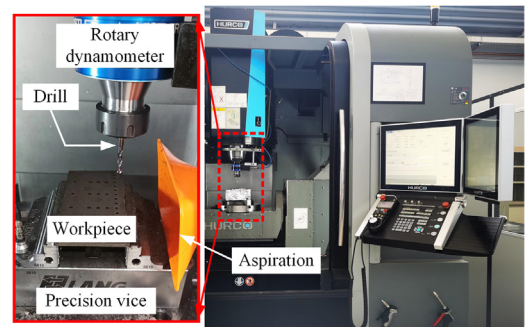


Fig. 2. Experimental set-up.

3.2. Numerical modelling

The sequence of the T800/M21 plate is $[0/90/45/-45/0]_4$, with the thickness of 0.25 mm for each ply [11]. Generic material properties of plies and interface are as listed in Table 1.

Table 1
Generic properties of T800/M21 ply and interface [13,14].

Property	Value	Property	Value
ρ (kg/m ³)	1590	$S_{12} = S_{13}$ (MPa)	106.48
E_{11} (GPa)	134.7	S_{23} (MPa)	69.4
$E_{22} = E_{33}$ (GPa)	7.7	G_{ff} (kJ/m ²)	340
$\nu_{12} = \nu_{13}$	0.369	G_{fc} (kJ/m ²)	60
ν_{23}	0.5	G_{mt} (kJ/m ²)	0.228
$G_{12} = G_{13}$ (GPa)	4.2	G_{mc} (kJ/m ²)	1
G_{23} (GPa)	2.5	t_n^0 (MPa)	75
X_t (MPa)	2290.5	$t_s^0 = t_t^0$ (MPa)	95
X_c (MPa)	1051	G_{tc} (kJ/m ²)	0.228
Y_t (MPa)	41.43	$G_{sc} = G_{tc}$ (kJ/m ²)	0.652
Y_c (MPa)	210		

For the numerical model, the thickness of 0.24 mm was used for the ply with elements C3D8R, and 0.01 mm for the interface with cohesive elements COH3D8. All plies were modelled as equivalent homogeneous materials. The drill was modelled as a rigid body with elements C3D10M with mechanical properties shown in Ref [9]. According to the mesh sensitivity test, results are influenced by both the shape and the size of the mesh, especially for cohesive elements. Therefore, fine meshes were assigned within the major deformation zone with smallest sizes of $0.15 \times 0.15 \times 0.12$ mm³. Coulomb friction law with coefficient 0.1 was used [12]. The boundary conditions and corresponding details of the proposed model are as shown in Fig. 3, and no back plates were used in both the experiments and the simulations. The time domains of the entire process were set as 0.6 s and 1.2 s to make sure that it can cover the entire process from the entry to the exit for both cases. Simulations were launched by 12 CPUs on a high performance workstation, and the estimated calculation time is

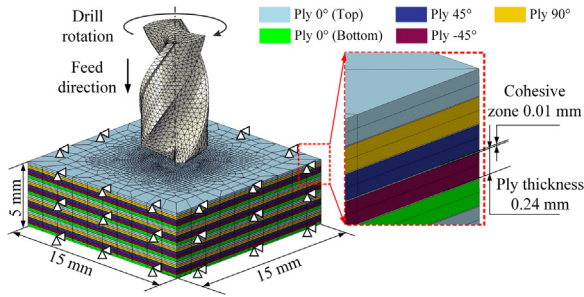


Fig. 3. Boundary conditions of the numerical model.

60 h.

4. Results and discussions

4.1. Variation of thrust forces and torques

Thrust forces and torques are the most common variables for validation of drilling models. These data were directly captured by the rotary dynamometer in the experimental work. As cohesive elements are applied in the model, they are assigned with a high modulus to avoid the numerical issues induced by the compression of those elements. In this case, abnormal high forces may be output at some material points and should be omitted, as recommended by Cepero-Mejías et al. [15]. Globally, it shows a good agreement between the experimental data and simulation results in terms of both thrust forces and torques, as shown in Fig. 4.

For both cutting conditions, the average prediction errors are about 7% for thrust forces and 10% for torques, respectively. At the same cutting speed, both thrust forces and torques increase with the

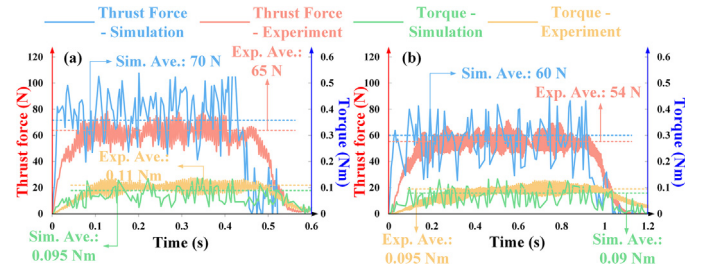


Fig. 4. Comparison of thrust forces and torques between experimental data and simulation results at different cutting conditions, (a) $V_c = 100$ m/min, $f = 0.1$ mm/rev, (b) $V_c = 100$ m/min, $f = 0.05$ mm/rev.

increase of feeds, while the increase of thrust forces is more apparent than that of torques. In addition, a more severe condition of delamination is expected at high feeds as thrust force is the key factor inducing delamination.

4.2. Delamination

Delamination is one of the most important concerns in terms of drilling CFRP, which is tightly related to thrust forces. It is also used for validating the proposed model. The delamination at exit is measured through tomography (model: μ CT-GE V|Tome|X-S), which shows a good agreement with simulation results (Fig. 5). For the final

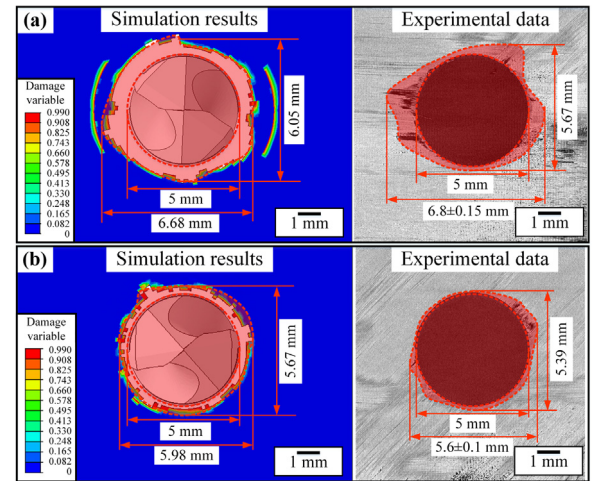


Fig. 5. Comparison of delamination at the exit between experimental data and simulation results at different cutting conditions, (a) $V_c = 100$ m/min, $f = 0.1$ mm/rev, (b) $V_c = 100$ m/min, $f = 0.05$ mm/rev. Red areas represent delamination affected areas.

interface close to the exit, the major damage propagates along both -45° and 0° corresponding to the plies orientations.

The global errors between the prediction and experiments in terms of damaged diameter induced by delamination are around 5–6%. Delamination factor F_d is determined following $F_d = D_d/D_0$, where D_0 is the drill diameter and D_d the damaged diameter. With higher feed of 0.1 mm/rev, the variable F_d can reach about 1.3, while with lower feed of 0.05 mm/rev, it decreases to the value smaller than 1.2. It follows the same trend as expected, which also verifies the accuracy and capabilities of the proposed model.

4.3. The degradation of mechanical properties in the hole surface

Although the four damage modes all participate in the material removal process, the fractions are quite different for each. Fiber compressive damage rarely occurs, while fiber tensile and matrix compressive modes mostly appear in the removed parts. Thereby, the matrix tensile damage is the most predominant mode reserved in the machined surfaces, as shown in Fig. 6.

As a result, major contributions to degradations of mechanical properties in the hole surface in terms of damage level of the stiffness

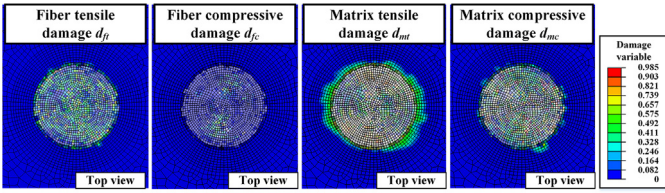


Fig. 6. Fractions of different damage modes after drilling at $V_c = 100$ m/min, $f = 0.1$ mm/rev. Gray parts represent the removed elements.

originate from the matrix tensile damage. The damaged parts show a strong dependency on the fiber orientation, as the matrix tensile damage can be induced by either the fiber pull-out or debonding. Different with interfacial damage, the degradation of stiffness matrix within the ply is only related to fiber orientation of the corresponding ply. With the defined damaged variable, the degradation of the mechanical properties can be evaluated by Eq. (7) through updating the stiffness matrix. Moreover, lower feed is beneficial for restraining the propagation of the degraded area at both the entry and the exit,

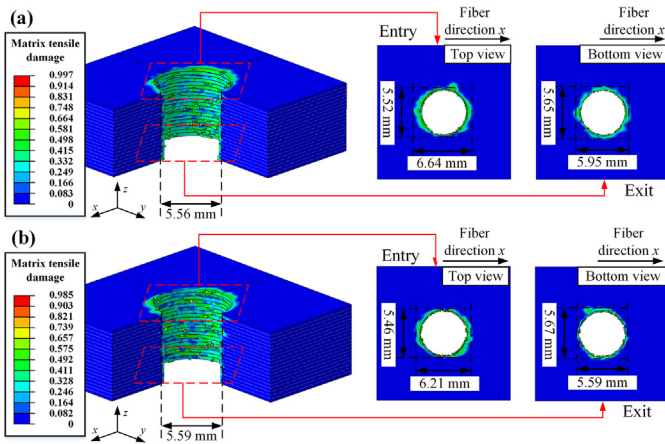


Fig. 7. Degradation areas in the hole surface under different cutting conditions, (a) $V_c = 100$ m/min, $f = 0.1$ mm/rev, (b) $V_c = 100$ m/min, $f = 0.05$ mm/rev.

although the maximum damage level and the average affected area throughout the hole are not changed significantly, as shown in Fig. 7.

The largest diameter 6.64 mm of the degraded area appears at the entry at $V_c = 100$ m/min, $f = 0.1$ mm/rev. The value is decreased to 6.21 mm when the feed decreases to 0.05 mm/rev. The average degraded diameters within the middle areas of the hole are similar for both cases, which are 5.56 mm and 5.59 mm, respectively. While for the damage level in the surface layer, it is not significantly influenced by cutting parameters. In most areas, the values range from 0.2 to 0.6, and the statistics of the two cutting conditions are summarized in Table 2.

Hence, following Eq. (7), the existence of matrix tensile damage within the hole surface induces a global degradation of all the terms of the stiffness matrix for more than 40% except C_{11} . Moreover, lower feeds are beneficial for controlling the size of degraded zones, although the effects on controlling the damage level are marginal. The restrain of degradation is based on the sacrifice of machining efficiency, although the hole integrity is always predominant over productivity for aeronautics industries. Nevertheless, it is still an

Table 2
Statistics of damage level for matrix tension in the hole surface.

Range of damage variable	Percentage $V_c = 100$ m/min, $f = 0.1$ mm/rev	$V_c = 100$ m/min, $f = 0.05$ mm/rev
$d_{mt} < 0.2$	23.7%	26.8%
$0.2 < d_{mt} < 0.4$	43.2%	42.8%
$0.4 < d_{mt} < 0.6$	30.7%	28.4%
$d_{mt} > 0.6$	2.4%	2%

important matter to be considered in order to balance the integrity and efficiency to enhance the global machining performance by optimizing cutting parameters.

5. Conclusions

In this study, a novel numerical model with progressive damage evolution laws was used to evaluate the degradation of mechanical properties in hole surfaces originating from permanent damage induced by drilling processes of CFRP. It reveals the fact that an average damage of 40% will be introduced to the stiffness of the hole surface, and its major cause is attributed to matrix tension. The level of damage in the hole surface is also dependent on drilling parameters, lower feeds leading to lower damage. Thus, it is of great significance towards optimization of cutting parameters concerning the functional performances of components. Currently the model only analysed the issues from mechanical perspectives, and fully coupled thermomechanical loadings should be merged in the future work to incorporate the impacts of tool wear as well as coolants into the optimization.

Declaration of Competing Interest

The authors declare that they have no known competing financial interests or personal relationships that could have appeared to influence the work reported in this paper.

Acknowledgments

The authors would like to acknowledge the complete funding from Institute Carnot ARTS and the drills provided by Tivoly company. The authors would also like to acknowledge Romain Brendlen from LaBoMaP and Matthieu Pedros from I2M for their kind assistances in preparations of the specimens.

References

- [1] Brinksmeier E, Fangmann S, Rentsch R (2011) Drilling of Composites and Resulting Surface Integrity. *CIRP Annals* 60(1):57–60.
- [2] Liu H, Birembaux H, Ayed Y, Rossi F, Poulachon G (2022) Recent Advances on Cryogenic Assistance in Drilling Operation: A Critical Review. *Journal of Manufacturing Science and Engineering* 144(10):100801.
- [3] Fleischer J (2018) Composite Materials Parts Manufacturing. *CIRP Annals* : 24.
- [4] M'Saoubi R, Axinte D, Soo SL, Nobel C, Attia H, Kappmeyer G, Engin S, Sim W-M (2015) High Performance Cutting of Advanced Aerospace Alloys and Composite Materials. *CIRP Annals* 64(2):557–580.
- [5] Van Der Sypt P, Chérif M, Bois C (2017) Analysis of the Fatigue Behaviour of Laminated Composite Holes Subjected to Pin-Bearing Loads. *International Journal of Fatigue* 103:86–98.
- [6] Zhang C, Li N, Wang W, Binienda WK, Fang H (2015) Progressive Damage Simulation of Triaxially Braided Composite Using a 3D Meso-Scale Finite Element Model. *Composite Structures* 125:104–116.
- [7] Isbilir O, Ghassemieh E (2013) Numerical Investigation of the Effects of Drill Geometry on Drilling Induced Delamination of Carbon Fiber Reinforced Composites. *Composite Structures* 105:126–133.
- [8] Wang G-D, Melly SK, Ahmed SKK (2018) Finite Element Study into the Effects of Fiber Orientations and Stacking Sequence on Drilling Induced Delamination in CFRP/Al Stack. *Science and Engineering of Composite Materials* 25(3):555–563.
- [9] Phadnis VA, Makhadmeh F, Roy A, Silberschmidt VV (2013) Drilling in Carbon/Epoxy Composites: Experimental Investigations and Finite Element Implementation. *Composites Part A: Applied Science and Manufacturing* 47:41–51.
- [10] Feito N, López-Puente J, Santiuste C, Miguélez MH (2014) Numerical Prediction of Delamination in CFRP Drilling. *Composite Structures* 108:677–683.
- [11] Bonnet C, Poulachon G, Rech J, Girard Y, Costes JP (2015) CFRP Drilling: Fundamental Study of Local Feed Force and Consequences on Hole Exit Damage. *International Journal of Machine Tools and Manufacture* 94:57–64.
- [12] Klinkova O, Rech J, Drapier S, Bergheau J-M (2011) Characterization of Friction Properties at the Workmaterial/Cutting Tool Interface during the Machining of Randomly Structured Carbon Fibers Reinforced Polymer with Carbide Tools under Dry Conditions. *Tribology International* 44(12):2050–2058.
- [13] Marín L, Trias D, Badalló P, Rus G, Mayugo JA (2012) Optimization of Composite Stiffened Panels under Mechanical and Hygrothermal Loads Using Neural Networks and Genetic Algorithms. *Composite Structures* 94(11):3321–3326.
- [14] Furtado C, Catalanotti G, Artero A, Gray PJ, Wardle BL, Camanho PP (2019) Simulation of Failure in Laminated Polymer Composites: Building-Block Validation. *Composite Structures* 226:111168.
- [15] Cepero-Mejías F, Curiel-Sosa JL, Blázquez A, Yu TT, Kerrigan K, Phadnis VA (2020) Review of Recent Developments and Induced Damage Assessment in the Modelling of the Machining of Long Fibre Reinforced Polymer Composites. *Composite Structures* 240:112006.